

Parabolic Mirror-Assisted Thermoelectric and Radiative Cooling System for Maximizing Power Generation Utilizing Solar and Outer Space Thermodynamic Resources

Ik Hoon Jeong, Sang Wook Park, Min Seong Kim, June Tae Kim, and Gil Ju Lee*

Radiative cooling technology is extensively researched as a green technology, leveraging outer space as a thermodynamic resource. Recently, integrating thermoelectric generators (TEGs) and radiative coolers (RCs) are proposed to generate power using the temperature difference between the ambient and the radiative cooler. However, current TEG-RC systems only utilize one thermodynamic resource, resulting in suboptimal efficiency. It proposes a parabolic mirror-assisted TEG-RC system that fully utilizes both the Sun and outer space as thermodynamic resources. The system places the hot side of the TEG, covered by a solar absorber (SA), at the focal point of the parabolic mirror, while the RC is located on the cold side of the TEG. Theoretical and experimental results reveal the optimal ratio between the RC and SA sizes to balance the power mismatch between cooling and heating powers. It also finds that the number of TEG stacks significantly affects power generation efficiency and determines the optimal number. Outdoor measurements demonstrate exceptional power generation during the daytime, which is an unprecedented achievement. This study also demonstrates the further enhancement in power generation efficiency when the proposed system is integrated with concentrated solar cells instead of the SA.

resource, leading to suboptimal efficiency.^[4,7,8] Figure 1a illustrates a conventional integrated system combining a RC and a TEG. The conventional TEG-RC systems generate electric power by exploiting the temperature difference between both sides of the TEG,^[9] facilitated by an ambient heat-absorbing process at the lower end and a heat-emitting process through the RC at the upper end.^[4,5,7] However, this temperature difference is relatively small (approximately 4°C),^[10–12] as the absorbed ambient heat is limited by surrounding conditions, causing the conventional system to produce lesser amount of electrical energy.^[5–10] To mitigate this downside, sunlight is used instead of ambient heat as the thermodynamic resource to heat up the hot side of the TEG and to enhance the electricity generation regardless of surrounding conditions. Nonetheless, maximizing both radiative cooling and solar absorption is hindered when the RC and TEG


1. Introduction

Radiative cooling technology has recently emerged as a promising sustainable energy solution, capitalizing on the cold temperature of outer space as a thermodynamic resource.^[1,2,3] The integration of thermoelectric generators (TEGs) with radiative coolers (RCs) has been proposed to generate electricity using thermal energy without additional other energy.^[4–6] However, current TEG-RC systems only exploit a single thermodynamic

face the sky, limiting the use of solar absorption in the TEG-RC system.^[13]

In response to these challenges, we propose a parabolic mirror-assisted TEG-RC system that harnesses both the Sun and outer space as thermodynamic resources. By incorporating a parabolic mirror, sunlight can be absorbed by a solar absorber (SA) covering the hot side of the TEG without interfering with the radiative cooling effect (Figure 1b).^[14,15] Generally, the powers emitted by radiative cooling and absorbed from sunlight are proportional to the size of the RC and SA, respectively. However, since the TEG-RC structure directly obstructs the portion of sunlight reaching the parabolic mirror, enlarging the area of the RC panel could diminish the amount of solar absorption at the SA placed on the bottom of the TEG device, thus deteriorating the power generation efficiency. In other words, a larger RC area could yield more heat emission from RC but less solar absorption at SA, resulting in an imbalance between the amount of emitted heat and absorbed heat. In this context, optimizing the size of the RC and SA is crucial to balance the power disproportion between heat emission and heat absorption (Figure 1c). This result presents a simulated comparison of incoming/outgoing powers according to the ratio of RC length (L_{RC}) and SA length (L_{SA}). For the

I. H. Jeong, S. W. Park, M. S. Kim, J. T. Kim, G. J. Lee
 Department of Electronics Engineering
 Pusan National University
 Busandaehak-ro 63, Geumjeong-gu, Busan46241, Republic of Korea
 E-mail: gjlee0414@pusan.ac.kr

 The ORCID identification number(s) for the author(s) of this article can be found under <https://doi.org/10.1002/admi.202300573>

© 2023 The Authors. Advanced Materials Interfaces published by Wiley-VCH GmbH. This is an open access article under the terms of the Creative Commons Attribution License, which permits use, distribution and reproduction in any medium, provided the original work is properly cited.

DOI: 10.1002/admi.202300573

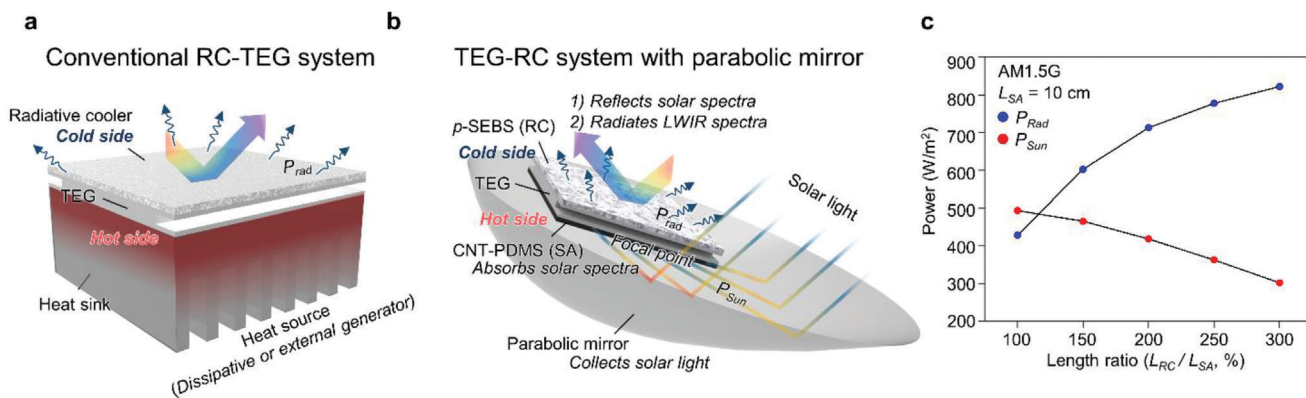


Figure 1. Comparison of conventional TEG-RC system and advanced TEG-RC system. a) Schematic diagram of a conventional TEG-RC system using the ambient heat as thermal source. b) Schematic illustration of the proposed TEG-RC system when Sunlight is heating source because light is converged to TEG by parabolic mirror. c) Trade-off by RC area that as length ratio is increasing, radiative power by the RC (i.e., P_{rad}) is increasing, however incident light power to the SA (i.e., P_{Sun}) is decreasing.

proposed system, excessive solar absorption significantly increases the temperature of the TEG when the areas of the RC and SA are equal (i.e., $L_{RC}/L_{SA} = 100\%$). The larger the radiative cooler area, the higher the radiant power (Figure 1c; P_{rad} , blue),^[4] but the smaller the absorbed solar power (Figure 1c; P_{Sun} , red). When L_{RC} and L_{SA} are equal (i.e., $L_{RC}/L_{SA} = 100\%$), P_{rad} is 4.28 W and P_{Sun} is 4.93 W. P_{rad} and P_{Sun} for L_{RC}/L_{SA} (150%, 200%, 250%, and 300%) are as follows: P_{rad} : 13.56, 28.51, 48.60, and 74.00 W. P_{Sun} : 4.65, 4.18, 3.63, and 3.02 W. Changing these values to $W\ m^{-2}$ yields Figure 1c. The incoming and outgoing powers exhibit a trade-off relationship.

Through theoretical and experimental analyses, we explore the optimal ratio between the RC and SA sizes to successfully mitigate the power mismatch. Moreover, we examine the influence of the number of vertical TEG stacks on power generation efficiency and optimize the stack count for the TEG-RC system.^[3,16,17] Our outdoor measurements showcase remarkable power generation (i.e., maximum $2.98\ W\ m^{-2}$) during the daytime, a previously unreported accomplishment. In addition, research on photovoltaic (PV)-TEG has been conducted in recent years.^[18–22] Our study gains further importance when the proposed system is integrated with concentrated solar cells in place of the SA,^[23] Consequently, the parabolic mirror-assisted TEG-RC system holds the potential to revolutionize sustainable energy generation by offering continuous power generation throughout the entire daytime.

2. Results and Discussion

2.1. The Analysis for RC, SA Films

Figure 2 presents the spectral and thermal characteristics for the RC and SA. Figure 2a displays a photograph and scanning electron microscope (SEM) images of the RC film, which is composed of porous Styrene Ethylene Butylene Styrene (*p*-SEBS) with numerous micro-scale air voids.^[2,24–28] Figure 2b depicts the pore size distribution in terms of diameters; their average and standard deviation values are 1.17 and 0.77 μm , respectively.^[29,30] Figure 2c presents the simulated scattering efficiency of the RC structure in terms of pore diameter and wavelength, indicating

that pores with a diameter over 1 μm effectively trigger Mie scattering in the solar spectrum.^[31,32] These abundant pores facilitate multiple Mie scattering, thus exhibiting near-unity reflectivity in the solar spectrum (0.3–2.5 μm).^[2] The detailed procedures for the optical simulation are demonstrated in the Experimental Section.

A mixture of carbon nanotube (CNT) and polydimethylsiloxane (PDMS) serves as the SA since CNTs function as an efficient blackbody material, absorbing electromagnetic wave with wavelengths ranging from ultraviolet to long-wave infrared.^[33–35] Additionally, the viscous nature of PDMS in its liquid state (before curing) is suitable for mixing with CNT powder. To optimize the SA, three samples with different CNT and PDMS weight ratios (i.e., 0.01, 0.05, and 0.08 wt%) were prepared.^[33] As depicted in Figure 2d, the sample with a higher CNT concentration exhibits a darker exterior, and a higher thermal equilibrium temperature ($\approx 44\ ^\circ\text{C}$) under direct sunlight.

The spectral optical characteristics of the RC and SA are described in Figure 2e, where reflectance and emissivity spectra are measured using an UV–vis–IR spectrophotometer and Fourier transform infrared spectroscopy (FTIR).^[36–39] As previously mentioned, the RC film exhibits multiple Mie scattering in the solar spectrum, resulting in near-unity reflectivity within this range denoted by “ R_{RC} ” (0.3–2.5 μm). Additionally, high emissivity in the atmospheric window (8–13 μm), denoted by “ E_{RC} ”, is observed due to the inherent material properties of SEBS.^[2,40] Consequently, the RC film can cool an object to sub-ambient temperatures owing to these spectral features. On the other hand, for the SA film, the strong absorption of CNTs in the solar spectrum results in near-perfect solar absorption denoted by “ E_{SA} ” (i.e., near-zero reflectivity in the solar spectrum).^[41] Figure 2f demonstrates the measured heating and cooling performances of the SA and RC, respectively. During the experiment, the ambient air temperature remains at $\approx 25\ ^\circ\text{C}$. The temperature of SA increases up to 15 $^\circ\text{C}$ above the ambient temperature, while the RC film temperature decreases up to 5 $^\circ\text{C}$ below the ambient air temperature. The fabricated films exhibit outstanding cooling and heating performance. Figure S7 (Supporting Information) specifies the detailed measurement setup, and the Experimental Section describes the fabrication procedures of the RC and SA films.

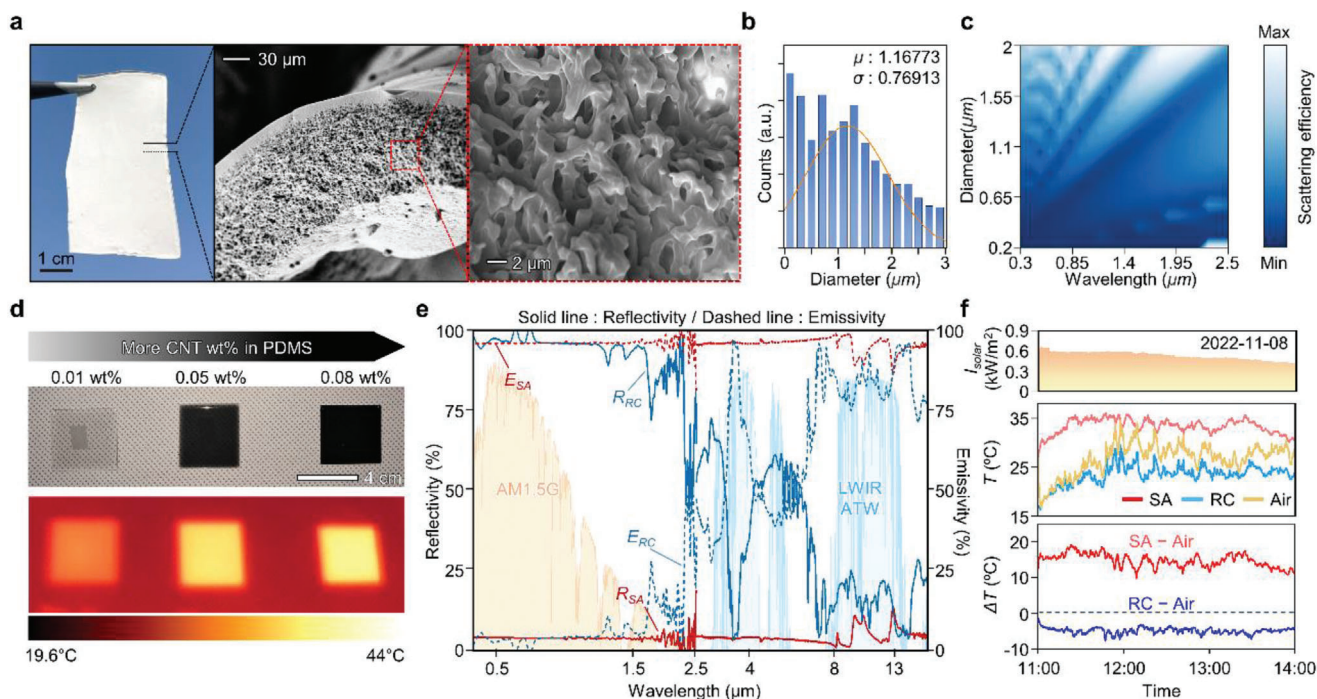


Figure 2. Optical and thermal characteristics of RC film and SA film a) Scanning electron microscope image (SEM) of RC film. It consists of a porous structure, which leads to Mie scattering. bc) Number of voids along to size in RC film and consequent scattering efficiency. d) The change of temperature under PDMS-CNT mixture (top) according to the carbon nanotube (wt%). Thermal image (bottom) of PDMS-CNT when fully exposed to Sunlight. e) Optical properties for Wavelength. Solid and dotted lines represent reflectance and emissivity, respectively. “ E_{SA} ” and “ E_{RC} ” mean the emissivity of SA and RC. “ R_{SA} ” and “ R_{RC} ” indicate the reflectivity of SA and RC. f) In specific declination angle (i.e., -17.31°), temperatures of RC film and SA film under direct Sunlight. When exposed to Sunlight for ≈ 2 h, SA is 15°C higher ($\approx 40^\circ\text{C}$) than ambient temperature ($\approx 25^\circ\text{C}$) and RC is $5\text{--}6^\circ\text{C}$ lower (i.e., $\approx 19\text{--}20^\circ\text{C}$) than ambient temperature.

2.2. Simulation About the Effect of Parabolic Mirror

To maximize the power generation of the TEG, each side of TEG (hot and cold) needs to satisfy two conditions.^[42] First, the cold side should face the sky for passive radiative cooling.^[13,43] Second, sunlight should be focused on the hot side to increase the density of sunlight. A parabolic mirror is designed to satisfy these two conditions. The parabolic mirror concentrates incident light into its focal point. However, the angle of incident light varies depending on the region. As a result, the sunlight is often obliquely incident. Therefore, the angle of sunlight incidence must be considered when designing the geometry of the parabolic mirror to maximize the collected sunlight absorbed by the hot side of TEG.

Figure 3a illustrates the mechanism for designing the parabolic mirror used in our TEG-RC system. The solar altitude angle depends on the declination angle, latitude angle, and hour angle and can be expressed by the following equation.

$$\Theta = \sin^{-1}(\sin \delta \sin \varphi + \cos \delta \cos \varphi \cos \alpha) \quad (1)$$

where Θ , δ , φ , and α are the solar altitude angle, declination angle, latitude angle, and hour angle, respectively. The declination angle (δ) is the angle between the sunlight and the equator. The value of δ is 0° at spring and fall (3/22 and 9/23) and $\pm 23.5^\circ$ at summer and winter (6/21 and 12/22), respectively (See Section S5, Supporting Information for the detailed contents). Given a

specific declination angle ($\delta = 0^\circ$) and latitude angle ($\varphi = 35^\circ$ in our region), the solar altitude angle (Θ) changes with the hour angle ($\alpha = -90^\circ\text{--}90^\circ$).^[44,45] When the hour angle is 0° , the focal point is located at the center (See Section S5, Supporting Information for the detailed contents).

Therefore, to maximize the efficiency of the TEG-RC system, the parabolic mirror is designed under the assumption that the hour angle is zero, thereby constructing a central focal point. In Figure 3a, during the spring and fall seasons, the solar altitude angle depends on the latitude angle ($\Theta = 90 - \varphi$). As our experiments are conducted at approximately a 35° latitude angle, the altitude angle maintains its value at $\approx 55^\circ$. As a result, when the parabolic mirror is tilted $\approx 35^\circ$, sunlight incidence becomes parallel to the axis of the parabolic mirror. The reflected sunlight then sufficiently converges on the focal point due to the characteristic of the parabolic. However, the hour angle (α) is tuning from -90° to 90° during the day.^[45] When the parabolic mirror is centrally facing the Sun at noon, the hour angle is 0° , while the rate of change of the altitude angle decreases closer to noon. Consequently, to compensate for the changing altitude angle, we conducted the experiment near noon, adjusting the direction of the parabolic mirror towards the Sun ($\alpha = 0^\circ$) every 15 min.

The ray-tracing simulation is used to analyze the optical path in a parabolic mirror-assisted system. Figure 3b demonstrates the mechanism of sunlight convergence for the designed parabolic mirror. The detected positional light irradiation profile shows that the light is concentrated at the focal point, as depicted in

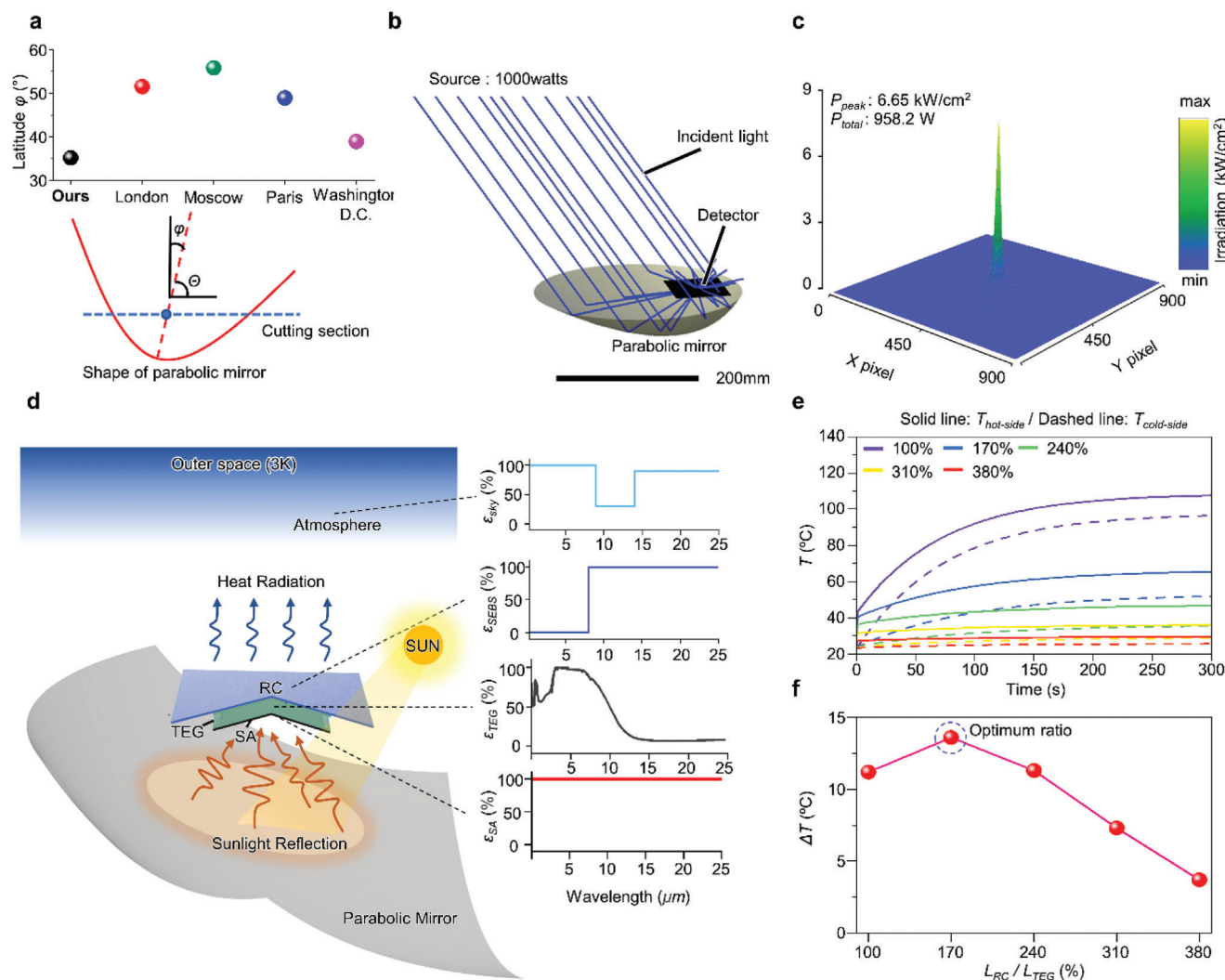


Figure 3. Simulation results of the proposed system. a) Parabolic mirror setting considering the position of the Sun by regions assumption that the declination angle (i.e., δ) is 0° and the hour angle of Sun (i.e., α) is 0° . Parabolic mirror is tilted by 35° in our case. b) Ray-tracing simulation of Sunlight reflected at the parabolic mirror. The incident lights are assumed to be parallel with the incident angle corresponding to AM1.5G configuration. The ray-tracing simulation confirms that the converging point of reflected Sunlight is located on the SA area. c) Analysis of irradiation intensity explains that light is converged on the converging point numerically. d) Schematic illustration of proposed system design. The graphs display the emissivity of the sky and materials. e) Simulated temperatures according to RC area as a function of time. f) Temperature difference (ΔT) depending on the size of TEG and RC.

Figure 3c. The concentration performance of the parabolic mirror is examined in Figure S8 (Supporting Information). Based on this optically optimized setup, a thermal simulation is conducted to calculate the temperature of the SA and RC over time, simultaneously accounting for both radiative cooling and solar absorption.

Along with the simulation, Figure S9 (Supporting Information) illustrates sunlight successfully converging at the focal point of our parabolic mirror in the experimental setup. Figure 3d presents the simulation model with the emissivity spectra of the sky and materials used in our proposed system. Figure 3e displays the temperature profiles for hot and cold sides of the TEG as a function of time, depending on the size. Figure 3f shows the temperature difference between the cold and hot sides of the TEG for several RC-SA length ratio configurations. The result in-

dicates that the temperature of the hot side of TEG diminishes as the RC size increases. Therefore, the optimal L_{RC}/L_{TEG} appears to be 170% for the largest temperature difference. Figure S10 (Supporting Information) presents the simulated temperatures depending on the emissivity profiles of RC and SA.

2.3. Indoor/Outdoor Experiments for Optimizing Power Generation System

Outdoor experiments were conducted to investigate the power generation efficiency depending on the size of the RC and SA, with the apparatus set as shown in Figure 4a. The experiments took place on the rooftop of the Department of Electronic Engineering building at Pusan National University

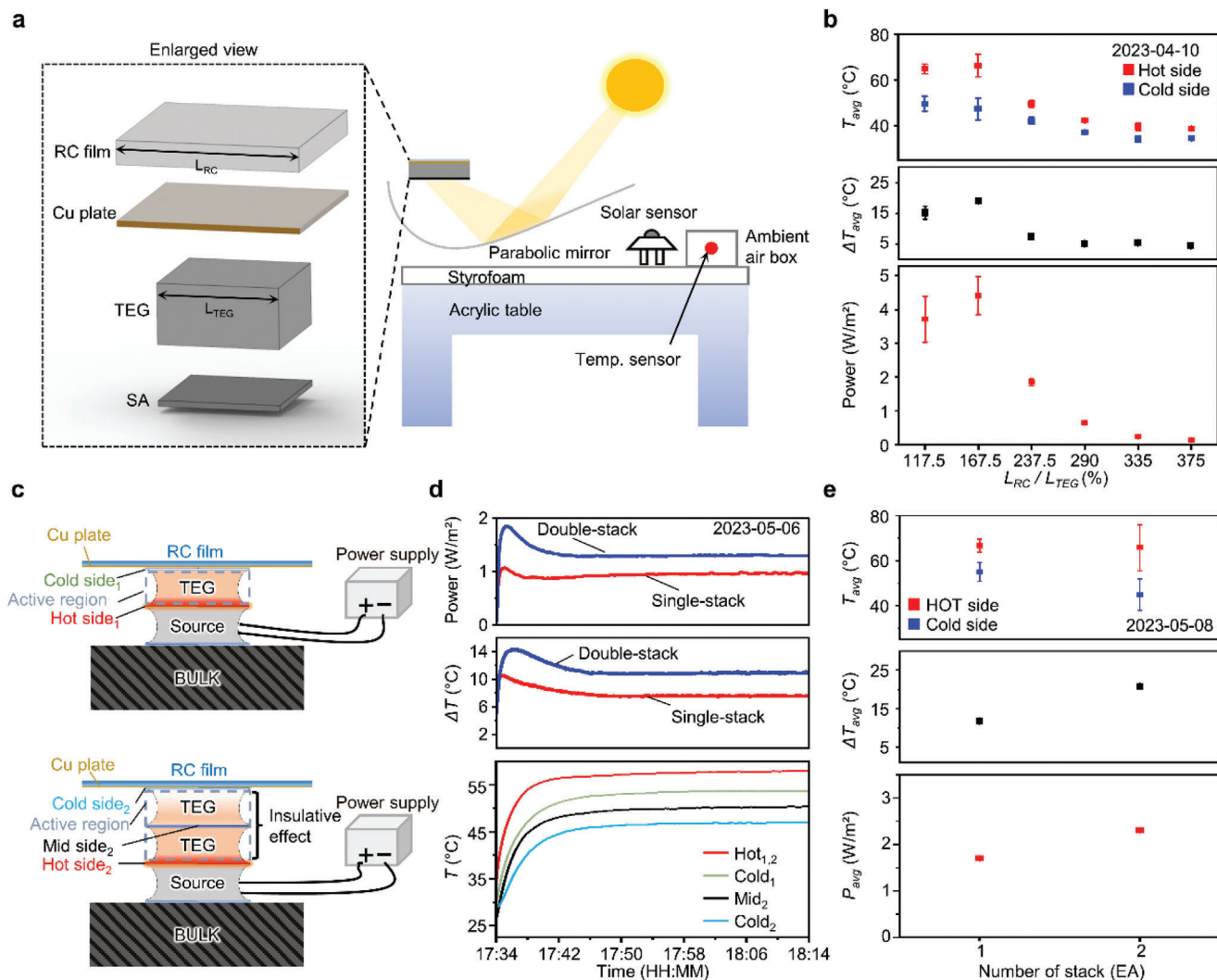


Figure 4. Optimization of RC area and TEG stacks. a) Schematic illustration of the outdoor experiment to optimize the size ratio of RC and TEG. b) In specific declination angle (i.e., 7.44°), measured average temperatures, generated power, and temperature difference of both sides of TEG in the experiment. Raw data are presented in Figure S11 (Supporting Information). Under the length ratio configuration of 167.5 (L_{RC}/L_{TEG} , %), the TEG-RC system exhibits highest temperature difference between lower and upper part of TEG, thus yields most efficient power generation. c) Schematic illustration of indoor experiment regarding the effect of number of TEG stacks. The thermal source is TEG device using Peltier effect, which converts electric energy to thermal energy. The applied voltage and current (i.e., 5 V 0.8A). d) Measured temperatures, temperature differences, and generated power about the indoor experiment. e) Under direct Sunlight, outdoor experiment measurement on average temperature, temperature difference, and generate power according to TEG stacks in specific declination angle (i.e., 16.90°). Figure S12 (Supporting Information) exhibits the raw data.

(latitude: 35.17955473°, longitude: 129.0756416°). The RC film and the upper side of the TEG were connected through a Cu plate with thermal tape, while the SA was adhered to the lower side of the TEG. Each layer was laminated with thermal tape to ensure stable bonding and sufficient heat transfer. A thermal insulator, Styrofoam, was placed on the acrylic table to prevent heat transfer from the ground. For the TEG, a commercial product was used in the experiment. Solar power and ambient temperature data were recorded using a pyranometer and an ambient air temperature sensor, respectively. The calculation of power generation by the TEG is explained in Section S1 (Supporting Information).

Figure 4b displays the generated power with different RC sizes (see Figure S11, Supporting Information for the details). The size of RC was manipulated along with that of the Cu plate. A com-

mercially available 15 × 15 cm² Cu plate was used. The size of the RC was set to match that of the Cu plate, with the RC attached to the Cu plate. The area of each Cu plate was proportionally reduced from the area of the original 225 cm² Cu plate (i.e., 80%, 60%, 40%, 20%, and 10%). This resulted in Cu plate areas of 180, 135, 90, 45, and 22.5 cm², respectively. Each plate was designed to be square-shaped, hence the lengths were 15, 13.4, 11.6, 9.5, 6.7, and 4.7 cm, respectively, with the length ratios of Cu plate to TEG (i.e., L_{RC}/L_{TEG}) being 375%, 335%, 290%, 237.5%, 167.5%, and 117.5%, respectively. Detailed methods for the cut-rate of Cu plate area and the length rate between TEG (i.e., 4 cm) and each Cu plate can be found in Figure S16 (Supporting Information).

Even though increasing the area of the RC leads to a lower temperature on the cold side of the TEG, it simultaneously

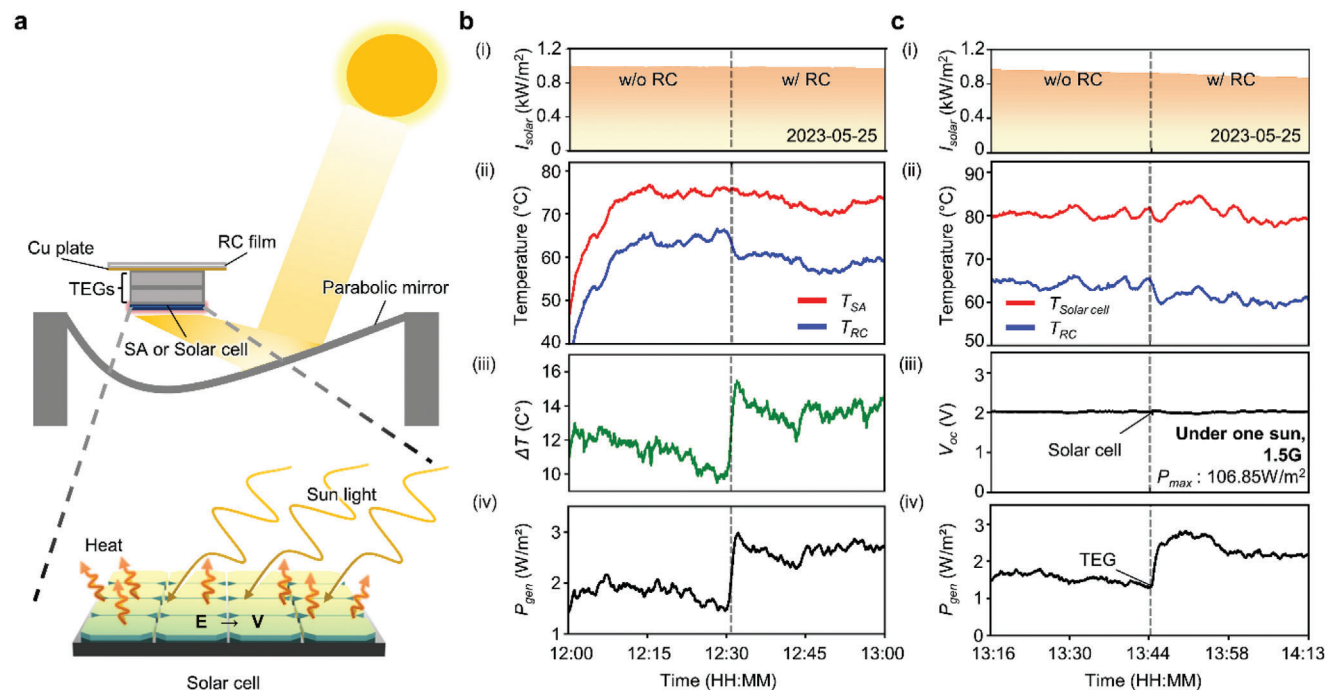


Figure 5. Temperature and power generation measured by the outdoor experiment setup in the daytime. a) System integrated with concentrated SA or solar cell. The power is generated by solar cell using the conversion of photons to electrons. Also, TEG generates an electricity using a residual heat due to solar cells. In specific declination angle (i.e., 20.87°), b) Measured temperature and generated power during the daytime. $L_{RC}/L_{TEG} = 167.5\%$ and two TEG stacks are used in the experiment. During experiment, the RC effect is introduced by removing Al foil. c) Measured temperature and open circuit voltage of solar cell and the power of TEG, that the photoelectric efficiency (i.e., η) is 10.06% and the maximum power (i.e., P_{max}) is 106.85 W m^{-2} . The solar cells places at the position of SA. As a result, temperature difference occurs due to solar cell and RC film.

reduces the amount of sunlight absorbed by the SA. Consequently, the amount of power generated tends to decrease significantly as the ratio of L_{RC}/L_{TEG} increases. To understand the reason for this phenomenon, outdoor measurements were conducted to examine the average temperature of the hot and cold sides, as well as the temperature difference (ΔT) between them, while changing the size ratio of RC and TEG (L_{RC}/L_{TEG}) from 117.5% to 375%. As the length ratio increases from 117.5%, the amount of heat emission at the RC also increases. This leads to a substantial temperature contrast between RC and SA, which peaks when the length ratio reaches 167.5%. However, as the length ratio continues to increase beyond this point, solar heat absorption decreases significantly. This reduction in heat absorption counteracts the temperature contrast between the hot and cold sides of the TEG-RC structure. Therefore, the experimental results suggest that the optimal length ratio between the RC and TEG is 167.5%.

The number of TEG stacks also has a significant impact on power generation efficiency, in addition to the size of the RC and SA. First, an indoor experiment was conducted to examine the effect of stacking using single and double-stacked TEGs under controlled experimental conditions (Figure 4c). These conditions included a constant ambient temperature and no climate influence. As a heat source, a TEG device was used on the bottom side of the setup, which produced thermal energy via Peltier effect that changes electric energy to thermal energy. The results of this indoor experiment are shown in Figure 4d. The same thermal energy was applied to each active layer due to the same elec-

tric energy provided by power supply (i.e., 5 V and 0.8A). The double-stacked TEGs showed a temperature difference of $\approx 11^\circ\text{C}$ between the cold and hot sides, while the single TEG had a difference of $\approx 8^\circ\text{C}$. The temperature on the cold side of double-stacked TEGs (Cold₂) was relatively lower than that of the cold side of the single TEG (Cold₁). The middle layer in the double-stacked TEG structure (Mid₂) functioned as a thermal insulator, increasing the temperature difference between the bottom hot side (Hot₂) and top cold side (Cold₂). The power generated by the two systems differed significantly, with approximated values of 1.2 and 0.9 W m^{-2} for the double-stacked TEGs and single TEG, respectively (see Section S2, Supporting Information for the details).

Furthermore, an outdoor experiment was carried out with single and double-stacked TEG-RC systems to demonstrate the effect of the number of TEGs. Figure 4e apparently shows the insulating effect of the middle layer in the double-stacked TEG-RC under direct Sunlight, resulting in a large temperature difference between the cold and hot sides (Top; Figure 4e). This increased temperature difference in the double-stacked TEG-RC led to a substantial increase in electricity generation. Figure S12 (Supporting Information), which shows an outdoor field test conducted with the optimal RC area and TEG stack number, demonstrates that the double-stacked TEG-RC generates more power (i.e., P_{avg} : 2.306 W m^{-2}) than the single-stacked TEG-RC power generation (i.e., P_{avg} : 1.7013 W m^{-2}).

Figure 5a illustrates the setup for an experiment that uses a double-stack system with the optimal RC film (as shown in

Figure S13, Supporting Information). This setup includes either the SA or the solar cell. Figure 5b shows the results from daytime experiments with the SA. Figure 5b-(ii) provides the recorded temperatures for both the RC and SA. During an outdoor field test, the effect of RC is initially removed by covering the RC film with aluminum foil (noted as “w/o RC”). This absence of RC effect causes the SA temperature increase to ≈ 76.5 °C due to the concentrated solar absorption. However, when the RC effect is reintroduced, the temperature difference between the cold and hot sides of the TEG increases from ≈ 11 to 14 °C (Figure 5b-(iii)). This increased temperature difference results in a larger amount of power generation (Figure 5b-(iv)). The proposed system, utilizing the RC effect, generates more power with a maximum value of 2.98 W m^{-2} , compared to the system covered with aluminum foil, which has maximum value of 2.1 W m^{-2} . For the thermoelectric efficiency, the efficiency with the RC effect is higher at an average of 0.756%, compared to that without the RC effect at an average 0.628%, as seen in Figure S14a. This increase in thermoelectric efficiency can be attributed to the rise in temperature difference (as detailed in Section S3, Supporting Information).^[46–48] Thus, the power generated in this system is significantly higher than that in a reported TEG-RC system, which generated 100 mW m^{-2} .^[8]

Figure 5c shows the results of an experiment in which a solar cell is used instead of the SA. The subsections (ii)–(iv) of Figure 5c illustrate the measured temperature, open circuit voltage of the solar cell, and power of the TEG, respectively. In the case of the commercial solar cell, with an average solar irradiance of $1061.515 \text{ W m}^{-2}$, the photoelectric efficiency (i.e., η) is 10.06% and the maximum power (i.e., P_{max}) is 106.85 W m^{-2} (detailed description is provided in Section S4, Supporting Information).^[49,50] Figure 5c-(ii) illustrates that the solar cell not only generates electric energy but also heat. The temperature of the solar cell ($T_{\text{Solar cell}}$) maintains ≈ 80 °C, as the double-stack of TEG provides thermal insulation between the solar cell and the RC film. However, the temperature on the cold side of the TEG is notably influenced by the RC. Consequently, the temperature of the RC (T_{RC}) experiences a drop of ≈ 5 °C when the RC effect is introduced. Throughout the experiment, the open circuit voltage of the solar cell remains at ≈ 2.1 V (Figure 5c-(iii)). The TEG power generation when influenced by the RC, reaching a maximum value of 2.75 W m^{-2} , surpasses the power generation that occurs without the effect of RC, which has a maximum of 1.79 W m^{-2} , as shown in Figure 5c-(iv).

When comparing the thermoelectric efficiency of the TEG, the efficiency when influenced by the RC, with an average of 1.06%, is superior to the efficiency without the influence of RC, with an average of 0.884%. This is demonstrated in Figure S14b and is a consequence of the increase in thermoelectric efficiency with the temperature difference, as described in Section S3 (Supporting Information). In short, the solar cell generates electricity by converting photons into electrons. Simultaneously, the TEG produces electricity by utilizing the RC film and the residual heat emitted from the solar cell.

3. Conclusion

In conclusion, our study reveals an innovative approach to harness wasted sunlight with a distinctive TEG-RC system. Using

cost-effective techniques, we developed films for solar absorption and radiative cooling. These films were designed to reflect and absorb the entire solar spectrum, leading to efficient solar absorption and radiative cooling, respectively. By adjusting the size of the RC, we managed to balance absorbed sunlight and heat release, thereby regulating the temperatures on both sides of the TEG. After rigorous theoretical and experimental efforts, an optimal ratio for RC length to TEG length was determined to be 167.5%. Our final experimental design yielded impressive results, with the solar absorber heating up to ≈ 76.5 °C and the RC maintaining a minimum temperature of 56.2 °C. The resulting temperature difference enabled us to generate a groundbreaking 2.98 W m^{-2} of power. Further, our research highlights the potential of incorporating concentrated solar cells into the system, enabling the recovery of wasted heat, and significantly boosting overall power generation. This advancement allows TEG-RC systems to generate power from photovoltaics and recover waste heat for additional electricity production. In addition, the application of the TEG-RC system in concentrated photovoltaic (CPV) systems shows promise. By harnessing the undesired intense heat from CPV, our proposed system could generate more electricity. Such additional electricity could be used to cool down the CPVs, mitigating the energy consumption used for cooling of CPV.^[51–53] In summary, this research challenges conventional TEG-RC systems, opening new horizons for energy-efficient innovations in solar power technology.

4. Experimental Section

Fabrication of RC/SA film: The RC film was fabricated through following two processes. First SEBS (Tuftec H1062, Asahi Kasei, Japan) beads, isopropyl alcohol (IPA), and chloroform (CHCl_3 ; C2432, Sigma-Aldrich, United States) were mixed in a mass ratio of 3.5:15.5:81 at room temperature, then sonicated for 1 h to sufficiently blend. Next, the SEBS solution was poured on a slide glass and left for 24 h to evaporate chloroform and IPA. The SEBS structure was chained with air voids to form the RC film.^[2]

The SA film comprises CNT powder (Sigma-Aldrich, United States) and PDMS (DC-184, DOW CORNING, United States). The film batch was prepared by dissolving the CNT into the PDMS with CNT 0.1wt% (10 g PDMS, 0.01 g CNT), blending with 1 g curling agent (SILASTIC RTV-4234-T4, DOW CORNING, United States), which makes the CNT-PDMS solidifying. The batch was then poured on the glass substrate (4 cm \times 4 cm). Ultimately, the CNT-PDMS sample was fabricated by inflicting the heat with the Hot plate (60 °C) for 8 h. The resultant sample exhibited flexible, resilient physical attributes.

Parabolic Mirror Modeling and Production: Under the 35° zenith assumption, as mentioned in Results and Discussion, parabolic mirror was manufactured by attaching reflective film on a 3D parabolic structure. The structure was modeled by first rotating a single parabola by its axis and defining its sweeping area. Then, the swept parabolic shape was tilted toward the Sun; zenith angle of 35° and cut with a plane that crosses the focal point of the tilted parabolic structure and parallel to the ground, which results the tilted pottery-like shaped structure. The entire modeling process was conducted with a commercial computer-aided design software (Rhinoceros 3D 5.0, Robert McNeel & Associates, USA), the commercial modeling utility, and the resultant parabolic structure is fabricated by 3D printer. Lastly, Aluminum foil as a reflective film was attached on the inner surface of the parabolic frame (Section S6, Supporting Information).

Optical/Thermal Simulation and Measurement Tool: Optical path of light reflected at parabolic mirror was confirmed by ray-tracing simulation (Zemax, Ansys, USA). Proper configurations of source, object, and detector were set for the efficient simulation. Rectangular light source was used

for the source in the simulation, which illuminates 10^7 rays of light. Previously modeled parabolic mirror was used for the object, and the axis of the mirror was directed toward the source. Detector was type of rectangular shape mimicking TEG, which was 1000×1000 pixels.

The pore structure and pore scattering efficiency were calculated with a commercial software, FullWAVE (Rsoft Design Group, Synopsys, United States) using FDTD theory (RSoft Design Group, Synopsys, United States). To estimate the temperature difference for the TEG hot-side/cold-side of proposed system, the software used the Heat Transfer (COMSOL Multiphysics, United States). Data visualization, noise adjustment, and scaling were performed using Python 3.10.5, Jupyter Notebook, and Origin programs. The SEM image analysis (i.e., pore diameter distribution) were performed using ImageJ.

The commercial TEG model (Tec1–12706) was used in the experiment, and the specific datasheet of the model was presented in Table S1 (Supporting Information). The thermograph (GL240, GRAPHTEC, Japan) was used to measure the temperature of the fabricated RC and SA films. Also, thermal imaging camera (AT300, IRay Technology Co., Ltd., China) was used for visual data. The solar power was measured using a commercial pyranometer (CMP3, Kipp & Zonen B.V., Netherlands).

Supporting Information

Supporting Information is available from the Wiley Online Library or from the author.

Acknowledgements

I.H.J. and S.W.P. contributed equally to this work. This work was supported by a 2-year Research Grant of Pusan National University.

Conflict of Interest

The authors declare no conflict of interest.

Data Availability Statement

The data that support the findings of this study are available from the corresponding author upon reasonable request.

Keywords

24 h electricity generation, radiative cooling, renewable energy, thermoelectric generator

Received: July 16, 2023
Published online:

- [1] W. Li, S. Fan, *Opt Photonics News* **2019**, *30*, 32.
[2] S. H. Byun, J. D. Yun, S. G. Heo, C. Shi, G. U. Lee, K.-C. Agno, K.-H. Jang, J. Xiao, Y. M. Song, J.-W. Jeong, *Adv. Sci.* **2022**, *9*, 2202549.
[3] D. H. Kim, S. Y. Heo, Y.-W. Oh, S. Jung, M. H. Kang, I.-S. Kang, G. J. Lee, Y. M. Song, *APL Photonics* **2023**, *8*, 030801.
[4] Z. Omair, S. Assaworrorarit, L. Fan, W. Jin, S. Fan, *iScience* **2022**, *25*, 104858.
[5] S. Assaworrorarit, Z. Omair, S. Fan, *Appl. Phys. Lett.* **2022**, *120*, 143901.
[6] F. J. DiSalvo, *Science* **1999**, *285*, 703.

- [7] Z. Zhan, M. ElKabbash, Z. Li, X. Li, J. Zhang, J. Rutledge, S. Singh, C. Guo, *Nano Energy* **2019**, *65*, 104060.
[8] L. E. Bell, *Science* **2008**, *321*, 1457.
[9] A. G. Olabi, M. Al-Murisi, H. M. Maghrabie, B. A. Yousef, E. T. Sayed, A. H. Alami, M. A. Abdelkareem, *Int. J. Thermofluids* **2022**, *16*, 100249.
[10] J. Liu, Y. Zhang, D. Zhang, S. Jiao, Z. Zhuofen, Z.-H. Zhou, *Energy Convers. Manage.* **2020**, *216*, 112923.
[11] B. Zhao, G. Pei, A. Raman, *Appl. Phys. Lett.* **2020**, *117*, 163903.
[12] E. Mu, Z. Wu, Z. Wu, X. Chen, Y. Liu, X. Fu, Z. Hu, *Nano Energy* **2019**, *55*, 494.
[13] M. d. M. Hossain, M. Gu, *Adv. Sci.* **2016**, *3*, 1500360.
[14] P. Oelhafen, A. Schüler, *Sol. Energy* **2005**, *79*, 110.
[15] D. Katzen, E. Levy, Y. Mastai, *Appl. Surf. Sci.* **2005**, *248*, 514.
[16] H. Lee, J. Sharp, D. Stokes, M. Pearson, S. Priya, *Appl. Energy* **2018**, *211*, 987.
[17] A. Montecucco, J. Siviter, A. R. Knox, *Appl. Energy* **2014**, *123*, 47.
[18] B. Zhao, M. Hu, X. Ao, Q. Xuan, Z. Song, G. Pei, *Sol. Energy Mater. Sol. Cells* **2021**, *228*, 111136.
[19] Z. Khalili, M. Sheikholeslami, *J. Magn. Magn. Mater.* **2023**, *580*, 170950.
[20] U. A. Saleh, M. A. Johar, S. A. B. Jumaat, M. N. Rejab, W. A. Wan Jamaludin, *Int. J. Renewable Energy Dev.* **2021**, *10*, 385.
[21] R. Bjørk, K. K. Nielsen, *Sol. Energy* **2015**, *120*, 187.
[22] C. Babu, P. Ponnambalam, *Energy Convers. Manage.* **2018**, *173*, 450.
[23] W. Li, Y. Shi, K. Chen, L. Zhu, S. Fan, *ACS Photonics* **2017**, *4*, 774.
[24] J. Mandal, Y. Fu, A. C. Overvig, M. Jia, K. Sun, N. N. Shi, H. Zhou, X. Xiao, N. Yu, Y. Yang, *Science* **2018**, *362*, 315.
[25] B. Xiang, R. Zhang, Y. Luo, S. Zhang, L. Xu, H. Min, S. Tang, X. Meng, *Nano Energy* **2021**, *81*, 105600.
[26] X. Yu, J. Chan, C. Chen, *Nano Energy* **2021**, *88*, 106259.
[27] H.-D. Wang, C.-H. Xue, X.-J. Guo, B.-Y. Liu, Z.-Y. Ji, M.-C. Huang, S.-T. Jia, *Appl. Mater. Today* **2021**, *24*, 101100.
[28] Y. Fu, J. Yang, Y. S. Su, W. Du, Y. G. Ma, *Sol. Energy Mater. Sol. Cells* **2019**, *191*, 50.
[29] P.-C. Hsu, A. Y. Song, P. B. Catrysse, C. Liu, Y. Peng, J. Xie, S. Fan, Y. Cui, *Science* **2016**, *353*, 1019.
[30] J. Liu, H. Tang, C. Jiang, S. Wu, L. Ye, D. Zhao, Z. Zhou, *Adv. Funct. Mater.* **2022**, *32*, 2206962.
[31] H. Xu, X. Chen, S. Ouyang, T. Kako, J. Ye, *J. Phys. Chem. C* **2012**, *116*, 3833.
[32] I. G. Yu, Y. J. Kim, H. J. Kim, C. Lee, W. I. Lee, *J. Mater. Chem.* **2011**, *21*, 532.
[33] J. Du, L. Wang, Y. Shi, F. Zhang, S. Hu, P. Liu, A. Li, J. Chen, *Sensors* **2020**, *20*, 4523.
[34] A. Mata, A. J. Fleischman, S. Roy, *Biomed. Microdevices* **2005**, *7*, 281.
[35] H.-C. Jung, J.-H. Moon, D.-H. Baek, J.-H. Lee, Y.-Y. Choi, J.-S. Hong, S.-H. Lee, *IEEE Trans. Biomed. Eng.* **2012**, *59*, 1472.
[36] F. Cao, K. McEnaney, G. Chen, Z. Ren, *Energy Environ. Sci.* **2014**, *7*, 1615.
[37] I. E. Khodasevych, L. Wang, A. Mitchell, G. Rosengarten, *Adv. Opt. Mater.* **2015**, *3*, 852.
[38] B. Zhao, M. Hu, X. Ao, N. Chen, G. Pei, *Appl. Energy* **2019**, *236*, 489.
[39] A. P. Raman, M. A. Anoma, L. Zhu, E. Rephaeli, S. Fan, *Nature* **2014**, *515*, 540.
[40] X. Li, B. Ma, J. Dai, C. Sui, D. Pande, D. R. Smith, L. C. Brinson, P.-C. Hsu, *Sci. Adv.* **2021**, *7*, abj7906.
[41] N. Selvakumar, S. B. Krupanidhi, H. C. Barshilia, *Adv. Mater.* **2014**, *26*, 2552.
[42] N. Jaziri, A. Boughamoura, J. Müller, B. Mezghani, F. Tounsi, M. Ismail, *Energy Rep.* **2019**, *6*, 264.

- [43] M. G. Meir, J. B. Rekstad, O. M. LØvvik, *Sol. Energy* **2002**, *73*, 403.
- [44] M. Blanco-Muriel, D. C. Alarcón-Padilla, T. López-Moratalla, M. Lara-Coira, *Sol. Energy* **2001**, *70*, 431.
- [45] S. Herrería-Alonso, A. Suárez-González, M. Rodríguez-Pérez, R. F. Rodríguez-Rubio, C. López-García, *Sensors* **2020**, *20*, 1391.
- [46] G. J. Snyder, T. S. Ursell, *Phys. Rev. Lett.* **2003**, *91*.
- [47] W. Vielstich, in *Handbook of Fuel Cells* (Eds: W. Vielstich, A. Lamm, H. A. Gasteiger, H. Yokokawa), Wiley, Hoboken, NJ **2010**, <https://doi.org/10.1002/9780470974001.f101004>.
- [48] D. Enescu, *Green Energy Advances*, InTech Open, London, UK **2019**.
- [49] M. Wang, X. Ma, W.-H. Huang, J. Liu, A. J. Curran, E. Schnabel, M. Koehl, K. O. Davis, J. Brynjarsdóttir, J. L. Braid, R. H. French, in *2018 IEEE 7th World Conference on Photovoltaic Energy Conversion (WCPEC) (A Joint Conference of 45th IEEE PVSC, 28th PVSEC & 34th EU PVSEC)*, IEEE, Waikoloa, HI **2018**
- [50] J. Yu, J. Fan, K. Lv, *Nanoscale* **2010**, *2*, 2144.
- [51] K. S. Reddy, S. Lokeshwaran, P. Agarwal, T. K. Mallick, *Energy Procedia* **2014**, *54*, 400.
- [52] B. Du, E. Hu, M. Kolhe, *Renewable Sustainable Energy Rev.* **2012**, *16*, 6732.
- [53] Y. M. Nandurkar, R. Shrivastava, V. K. Soni, *J. Inst. Eng. (India): C* **2022**, *103*, 259.